

Magnetic properties of $\text{RE}_2\text{O}_2\text{CO}_3$ (RE = Pr, Nd, Gd, Tb, Dy, Ho, Er, Yb) with a rare earth-bilayer of triangular lattice

Aya Rutherford, Chengkun Xing, and Haidong Zhou*

Department of Physics and Astronomy, University of Tennessee, Knoxville, TN 37996, USA

Qing Huang

Department of Physics and Astronomy, Louisiana State University, Baton Rouge, Louisiana 70803, USA

Eun Sang Choi

National High Magnetic Field Laboratory, Florida State University, Tallahassee, FL 32310, USA

Stuart Calder

Neutron Scattering Division, Oak Ridge National Laboratory, Oak Ridge, Tennessee 37831, USA

(Dated: July 12, 2024)

Polycrystalline samples of $\text{RE}_2\text{O}_2\text{CO}_3$ (RE = Pr, Nd, Gd, Tb, Dy, Ho, Er, and Yb) with a unique rare-earth bilayer of triangular lattice were synthesized and studied by DC and AC magnetic susceptibility. Data reveals various magnetic ground states including (i) a nonmagnetic ground state for the Pr sample; (ii) long range magnetic ordering for the Nd, Gd, Tb, Dy, Ho, and Er samples. Besides the Gd sample, they exhibit field-induced spin state transitions. More interestingly, the series spin state transitions in the Nd and Dy samples could be attributed to the field-induced up-up-down (UUD) spin structure. Neutron powder diffraction (NPD) measurements of the Er sample suggest a spiral spin structure below its T_N ; and (iii) a short range ordering for the Yb sample. The disrupted inter-layer interaction due to the shift of Yb^{3+} ions within the bilayer prevents long range magnetic ordering down to 30 mK and makes it another Yb-related triangular lattice antiferromagnet that has the potential to realize a quantum spin liquid state.

DOI:

I. INTRODUCTION

Rare-earth triangular lattice antiferromagnets (RE-TLAF) have attracted great interest in recent years. This fervor can be attributed to two of their characteristic elements: first, the triangular lattice, which is one of the simplest geometrically-frustrated lattices [1–5]. Second, the large spin-orbit coupling (SOC) and crystal electric field (CEF) effects of the RE ions' $4f$ electrons, which can lead to highly anisotropic exchange interactions [6, 7]. This combination makes RE-TLAFs an excellent platform for exploring exotic magnetic properties.

One driving force in the study of RE-TLAFs is the search for the quantum spin liquid (QSL), a highly spin-entangled state that is unable to attain magnetic ordering down to ultra-low temperatures [5, 8–12]. Most efforts have been focused on Ytterbium-based TLAFs as their easy-plane anisotropy and the $J_{\text{eff}} = \frac{1}{2}$ ground state of Yb^{3+} ions have the potential to realize the QSL state. Indeed, several Yb-TLAFs, including NaYbO_2 [13–18], NaYbS_2 [19–21], NaYbSe_2 [22–28], CsYbSe_2 [29–33], YbBO_3 [34–36], YbMgGaO_4 [37–42], $\text{YbZn}_2\text{GaO}_5$ [43], $\text{K}_3\text{Yb}(\text{VO}_4)_2$ [44], and $\text{Ba}_6\text{Yb}_2\text{Ti}_4\text{O}_{17}$ [45, 46], have been studied as QSL candidates. More recently, it was noticed that dominant Ising-like exchange interactions also can lead to a QSL state in RE-TLAFs, such as

in $\text{NdTa}_7\text{O}_{19}$ [47], CsNdSe_2 [48, 49], KTmSe_2 [50], and $\text{PrBa}_{11}\text{O}_{19}$ (B = Mg, Zn) [51, 52]. The Tm^{3+} and Pr^{3+} ions of KTmSe_2 and $\text{PrBa}_{11}\text{O}_{19}$ are non-Kramers ions whose doublet ground states usually split into two singlets. The spin-spin interaction can serve as a local exchange field on top of the double singlets. Therefore, their magnetic properties can be mapped to an Ising model in a transverse magnetic field. Moreover, while the magnetic exchange interaction is weak, the dipolar interaction of RE ions could also drive a system to a liquid-like state in RE-TLAFs, such as in $\text{NaBaYb}(\text{BO}_3)_2$ [53], $\text{KBaYb}(\text{BO}_3)_2$ [54, 55], and $\text{Ba}_3\text{Yb}(\text{BO}_3)_3$ [56].

Other interesting topics associated with RE-TLAFs include (i) proximate QSL behavior in a system with low temperature long-range magnetic ordering, for example in KYbSe_2 [57, 58]; (ii) the spin liquid state and topological structural defects in hexagonal TbInO_3 [59–63]; (iii) the Berezinskii-Kosterlitz-Thouless (BKT) phase with a quantum critical point, which has been proposed for TmMgGaO_4 [64–70] and $\text{Ba}_3\text{Gd}(\text{BO}_3)_3$ [71]; (iv) long range magnetic ordered states with rare spin structures, such as the stripe order observed in CsCeSe_2 [49] and KerSe_2 [72] and the realization of a two-sublattice exchange in $\text{Ba}_3\text{Er}(\text{BO}_3)_3$ [73]; and, (v) the interplay between the frustrated magnetism and charge carriers in metallic CeCd_3P_3 [74, 75] and semiconductor EuCd_2As_2 [76–80].

$\text{RE}_2\text{O}_2\text{CO}_3$ [81–84] is a family of compounds with rare earth triangular lattice bilayers that has been little studied as of yet. Magnetic properties of RE = Nd,

* hzhou10@utk.edu

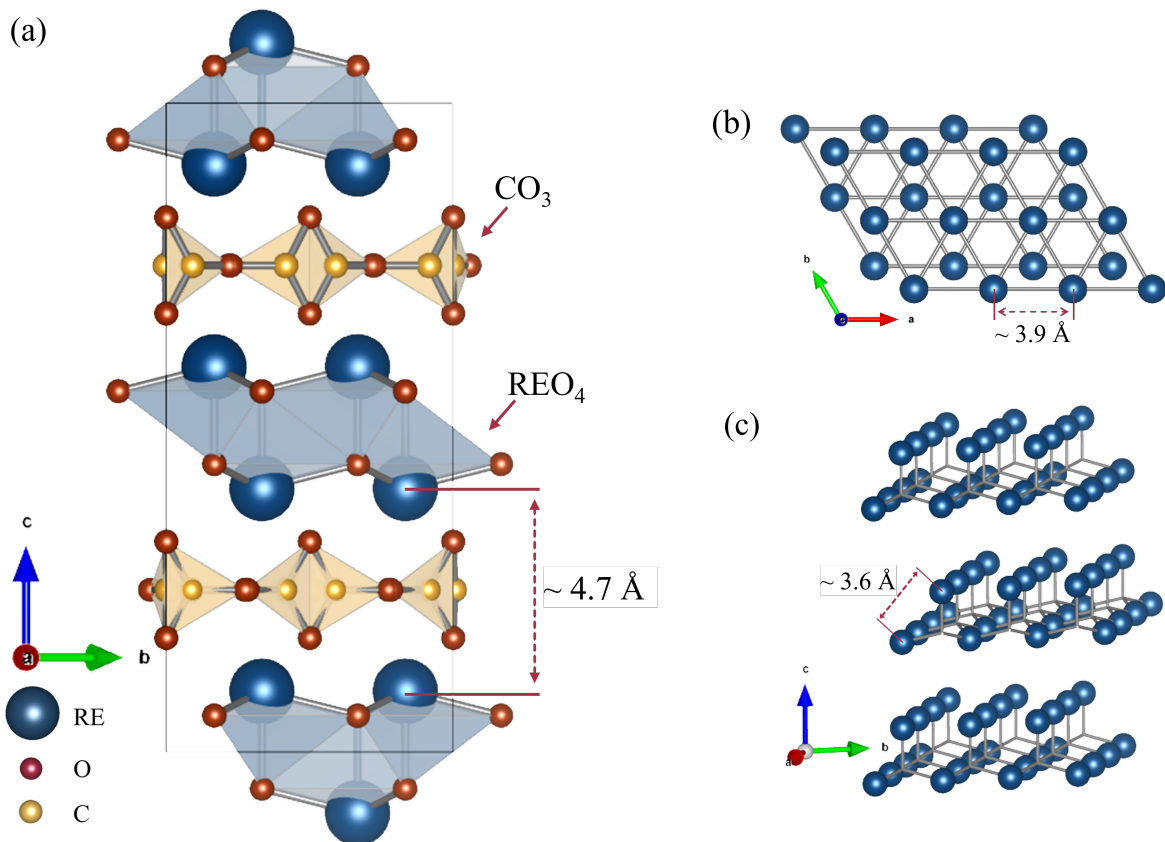


FIG. 1. (a) Crystal structure of $\text{RE}_2\text{O}_2\text{CO}_3$. (b) Arrangement of RE^{3+} ions in a triangular lattice bilayer. (c) Arrangement of RE^{3+} ions in shifted triangular lattice layers along the c -axis.

Sm, and Dy have been briefly reported but their magnetic phase diagrams have not been described [7]. Meanwhile, the magnetic properties of the other RE members are still unknown. In this paper, we synthesized and reported the magnetic ground states and magnetic phase diagrams of eight $\text{RE}_2\text{O}_2\text{CO}_3$ members (RE = Pr, Nd, Gd, Tb, Dy, Ho, Er, and Yb) by measuring DC and AC magnetic susceptibility. We also performed neutron powder diffraction (NPD) measurements on the Er sample.

II. EXPERIMENTAL DETAILS

Polycrystalline samples of $\text{RE}_2\text{O}_2\text{CO}_3$ (RE = Pr, Nd, Gd, Tb, Dy, Ho, Er, Yb) were synthesized in a two-step process. First, appropriate amounts of $\text{RE}(\text{NO}_3)_3 \cdot X\text{H}_2\text{O}$ and NaHCO_3 were dissolved in water to form a white precipitate. Then, this precipitate was filtered and annealed in a vacuumed and sealed quartz tube at temperatures of 550°C , 500°C , 375°C , 305°C , 370°C , 360°C , 340°C , 295°C for Pr, Nd, Gd, Tb, Dy, Ho, Er, Yb, respectively, for 24 to 36 hours.

The phase purity of the resulting polycrystalline samples was checked via room-temperature powder x-ray diffraction (XRD) using a HUBER imaging plate Guinier

camera 670 with Cu radiation ($\lambda = 1.54059 \text{ \AA}$). The XRD refinements were performed with the FULLPROF program. The crystal structures were plotted and the bond distances were computed using VESTA. DC magnetic susceptibility and magnetization were measured in a Physical Property Measurement System (PPMS) from Quantum Design with the vibrating sample magnetometer (VSM) option equipped. The DC magnetic susceptibility was measured at a magnetic field $B = 0.1 \text{ T}$ from 2 to 300 K and the DC magnetization was measured at 2 K from 0 to 12 T. The AC susceptibility measurements were conducted with a voltage-controlled current source (Stanford Research, Model CS580) and lock-in amplifier (Stanford Research, Model SR830) [85]. The RMS amplitude of the AC excitation field was set to be 0.6 Oe with the frequency between 80 Hz to 2147 Hz. The measurements were performed at SCM1 and SCM2 of the National High Magnetic Field Laboratory, Tallahassee.

The neutron powder diffraction (NPD) measurement was performed at the Neutron Powder Diffractometer (HB-2A) at HFIR, ORNL to study the nuclear and magnetic structure of $\text{Er}_2\text{O}_2\text{CO}_3$ [86]. A powder sample weighing approximately 0.5 grams was prepared for the experiment. The nuclear structure was studied by NPD measurements with 1.54 \AA neutron wavelength to ensure

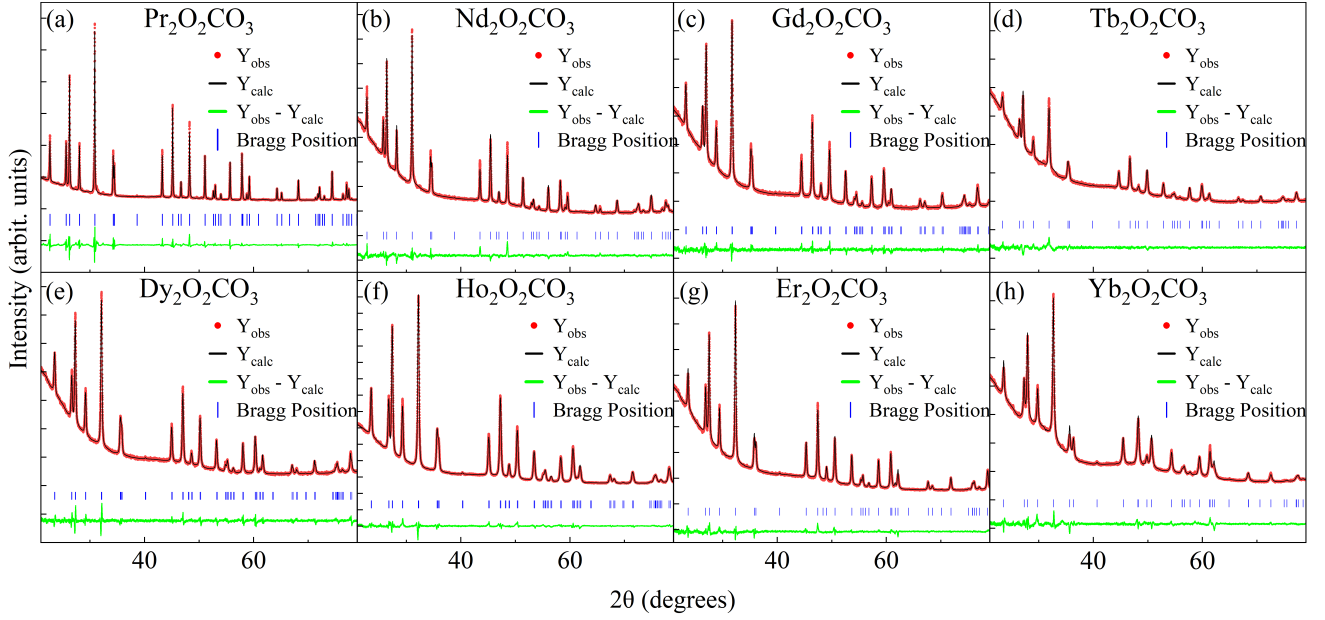


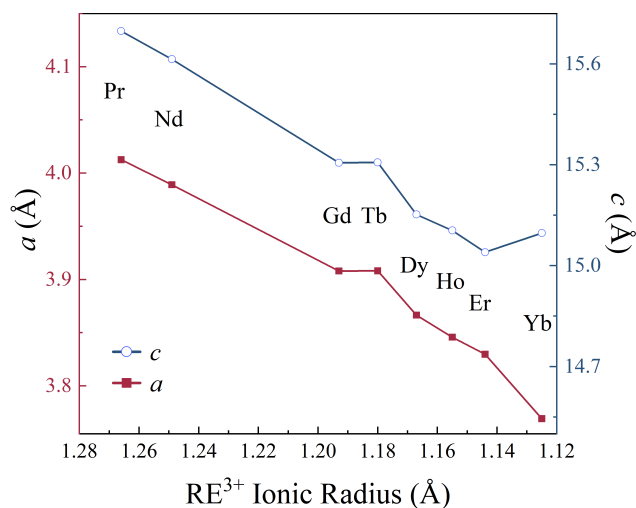
FIG. 2. Room temperature powder XRD patterns and best fits from Rietveld refinement.

TABLE I. Summary of room-temperature XRD Rietveld refinements for $\text{RE}_2\text{O}_2\text{CO}_3$.

RE	Pr	Nd	Gd	Tb	Dy	Ho	Er	Yb
RE^{3+} IR (Å)	1.126	1.109	1.053	1.040	1.027	1.015	1.004	0.985
a (Å)	4.01240(1)	3.98902(1)	3.90984(1)	3.88567(2)	3.86389(1)	3.84738(1)	3.82963(1)	3.76977(2)
c (Å)	15.69711(4)	15.61398(8)	15.31344(9)	15.23047(12)	15.14404(10)	15.11306(6)	15.03997(6)	15.09768(12)
RE	$(\frac{1}{3}, \frac{2}{3}, z)$	$(\frac{1}{3}, \frac{2}{3}, z)$	$(\frac{1}{3}, \frac{2}{3}, z)$	$(\frac{1}{3}, \frac{2}{3}, z)$	$(\frac{1}{3}, \frac{2}{3}, z)$	$(\frac{1}{3}, \frac{2}{3}, z)$	$(\frac{1}{3}, \frac{2}{3}, z)$	$(\frac{1}{3}, \frac{2}{3}, z)$
z	0.09484(3)	0.09496(3)	0.09417(3)	0.09415(4)	0.09397(4)	0.09358(2)	0.09352(2)	0.09242(4)
C	$(x, 2x, \frac{1}{4})$	$(x, 2x, \frac{1}{4})$	$(x, 2x, \frac{1}{4})$	$(x, 2x, \frac{1}{4})$	$(x, 2x, \frac{1}{4})$	$(x, 2x, \frac{1}{4})$	$(x, 2x, \frac{1}{4})$	$(x, 2x, \frac{1}{4})$
x	0.06006(8)	0.42056(4)	0.06017(3)	0.07208(1)	0.06850(6)	0.02017(6)	0.08791(5)	0.08841(5)
y	0.12021(16)	0.84114(8)	0.12048(6)	0.14429(2)	0.13710(12)	0.04041(12)	0.17591(10)	0.17692(10)
O ₁	$(\frac{1}{3}, \frac{2}{3}, z)$	$(\frac{1}{3}, \frac{2}{3}, z)$	$(\frac{1}{3}, \frac{2}{3}, z)$	$(\frac{1}{3}, \frac{2}{3}, z)$	$(\frac{1}{3}, \frac{2}{3}, z)$	$(\frac{1}{3}, \frac{2}{3}, z)$	$(\frac{1}{3}, \frac{2}{3}, z)$	$(\frac{1}{3}, \frac{2}{3}, z)$
z	0.55722(21)	0.55477(21)	0.55661(19)	0.55351(24)	0.55628(22)	0.55698(10)	0.55638(17)	0.55285(27)
O ₂	$(0, 0, z)$	$(0, 0, z)$	$(0, 0, z)$	$(0, 0, z)$	$(0, 0, z)$	$(0, 0, z)$	$(0, 0, z)$	$(0, 0, z)$
z	0.17920(35)	0.17358(36)	0.16921(38)	0.17357(51)	0.18052(34)	0.17474(17)	0.18251(26)	0.17653(37)
O ₃	$(x, 2x, \frac{1}{4})$	$(x, 2x, \frac{1}{4})$	$(x, 2x, \frac{1}{4})$	$(x, 2x, \frac{1}{4})$	$(x, 2x, \frac{1}{4})$	$(x, 2x, \frac{1}{4})$	$(x, 2x, \frac{1}{4})$	$(x, 2x, \frac{1}{4})$
x	0.20692(2)	0.10443(2)	0.23751(1)	0.23751(1)	0.23909(3)	0.23686(2)	0.24315(2)	0.21784(5)
y	0.41385(5)	0.20886(4)	0.46943(3)	0.47502(3)	0.47818(6)	0.47371(4)	0.48629(4)	0.43568(10)
R_p	2.77	1.26	1.05	1.16	1.19	1.59	1.36	1.49
R_{wp}	4.20	1.90	1.45	1.59	1.77	2.28	1.96	2.14
χ^2	20.3	4.20	3.28	3.06	4.39	5.64	3.94	4.92

TABLE II. Summary of magnetism parameters for RE₂O₂CO₃.

Compound	Low T θ_{CW} (K)	Low T $\mu_{\text{eff}}^{\text{exp}}$ (μ_B)	High T θ_{CW} (K)	High T $\mu_{\text{eff}}^{\text{exp}}$ (μ_B)	$\mu_{\text{eff}}^{\text{theo}}$ (μ_B)	M_{12T} (μ_B/RE^{3+})	M_S (μ_B/RE^{3+})
Pr ₂ O ₂ CO ₃	-37.32	3.62	-49.71	3.48	3.58	—	3.20
Nd ₂ O ₂ CO ₃	-4.13	2.66	-48.51	3.79	3.62	1.295	3.27
Gd ₂ O ₂ CO ₃	—	—	-5.42	-8.97	7.94	9.14	7.00
Tb ₂ O ₂ CO ₃	-6.70	8.85	-9.06	9.52	9.72	4.39	9.00
Dy ₂ O ₂ CO ₃	-8.70	9.33	-1.30	10.20	10.65	5.48	10.0
Ho ₂ O ₂ CO ₃	-6.83	9.41	-0.19	9.67	10.61	5.28	10.0
Er ₂ O ₂ CO ₃	-4.00	7.35	-2.94	7.85	9.58	4.00	9.00
Yb ₂ O ₂ CO ₃	-0.94	3.25	-44.25	4.39	4.54	1.80	4.00

FIG. 3. Lattice parameters obtained from Rietveld refinements as a function of the RE³⁺ ionic radius.

a larger Q coverage. Further measurements with a 2.41 Å neutron wavelength were utilized to focus on the magnetic signal in the low Q range. The diffraction data was analyzed by the Rietveld refinement technique within the FULLPROF program package.

III. STRUCTURE

All members of the RE₂O₂CO₃ family are isostructural and crystallize into the hexagonal space group P6₃/mmc. There are several distinct structural features. First, the corner-sharing REO₄ tetrahedra network in the *ab* plane forms an isotropic RE-triangular layer (Fig. 1). Second, each REO₄ tetrahedron is edge-sharing with three other tetrahedra of the adjacent layer along the *c*-axis, thus forming a RE-triangular lattice bilayer. The bilayers are separated from each other by carbonate groups along the *c*-axis. Third, very importantly, within each bi-

layer, the two RE-triangular lattices are displaced with respect to each other in such a way that the RE ion in one layer is projected towards the center of the triangle formed by the RE ions in the adjacent layer along the *c* axis, as shown in Fig. 1(b, c).

The XRD patterns for RE₂O₂CO₃ (RE = PR, Nd, Gd, Tb, Dy, Ho, Er, and Yb) with the refinement results superimposed on the data are shown in Fig. 2 and the experimental patterns agree well with the calculated ones. The structural refinement results are provided in Table I. Figure 3 shows the lattice parameters *a* (left axis) and *c* (right axis) versus ionic radius (IR) of the RE³⁺ ions. The lattice constants decrease approximately linearly with decreasing ionic radius. One anomaly is Yb₂O₂CO₃, which shows an unexpected larger *c* lattice parameter. Generally, the nearest neighbor distance for RE ions on a triangular layer is around 3.9 Å, the nearest distance between RE ions on adjacent RE-triangular layers within each bilayer is around 3.6 Å, and the distance between two adjacent bilayers along the *c*-axis is around 4.7 Å, as plotted in Fig. 1.

IV. MAGNETIC PROPERTIES

The DC magnetic susceptibility and DC magnetization data of all eight samples are shown in Fig. 4 and 5, respectively. The Curie Weiss (CW) law, $1/\chi = \frac{T - \theta_{CW}}{C}$ was used to fit the inverse susceptibility at both the high temperature regime [150 - 300 K] and low temperature regime [5 - 15 K]. The obtained Curie-Weiss temperatures θ_{CW} , and effective moments μ_{eff} are listed in Table II with the theoretically calculated free ion moment for comparison. The theoretical saturation moment $M_s = g_{\text{theo}}J$, where g_{theo} is the expected *g* factor for free-ions and *J* is the theoretical Hund's value, and the experimental saturation value at 12 T, M_{12T} , are also listed in Table II. Here, we assume that the magnetization value at 12 T (M_{12T}) is approaching saturation. Due to the linear increase of the magnetization at high field (Fig. 5), it is difficult to exactly extract the saturation moment.

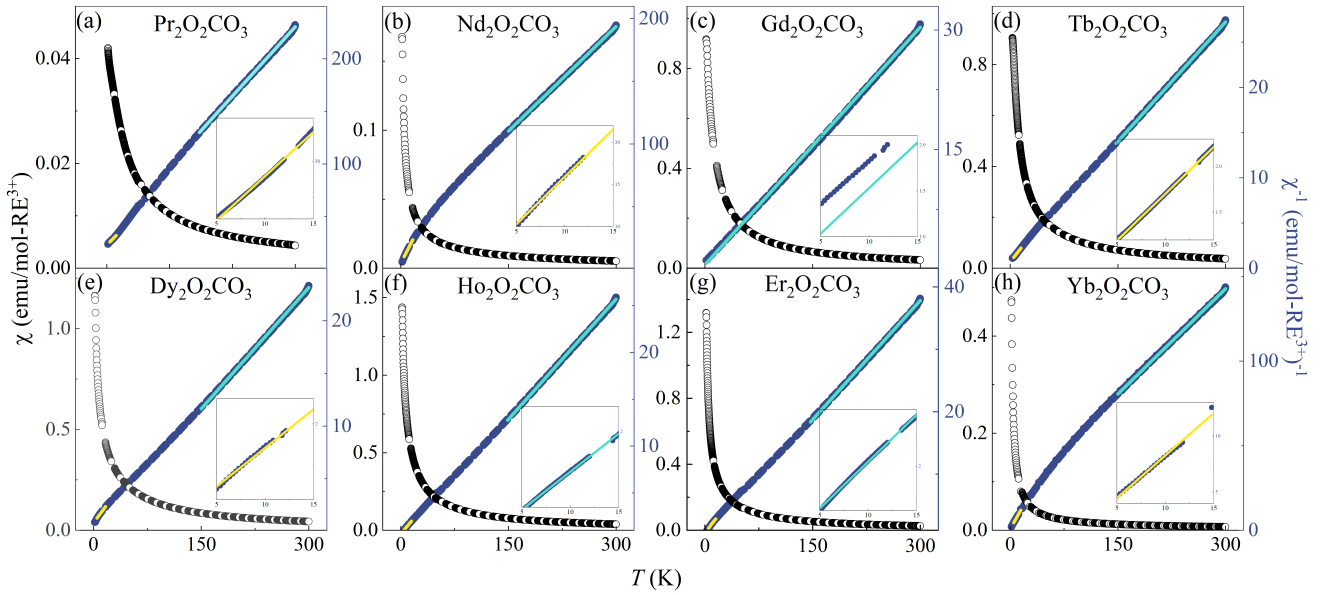


FIG. 4. DC susceptibility χ (left axis) and its inverse χ^{-1} (right axis) from 2 to 300 K at 0.1 T for $\text{RE}_2\text{O}_2\text{CO}_3$. High temperature (150–300 K) fits of inverse susceptibility are blue, low temperature (5–15 K) fits are yellow. Insets: χ^{-1} at low-temperature regions (5–15 K). The Curie-Weiss fit of $\text{Gd}_2\text{O}_2\text{CO}_3$ was instead over the entire temperature regime (2–300 K) in blue, with inset of the low temperature region.

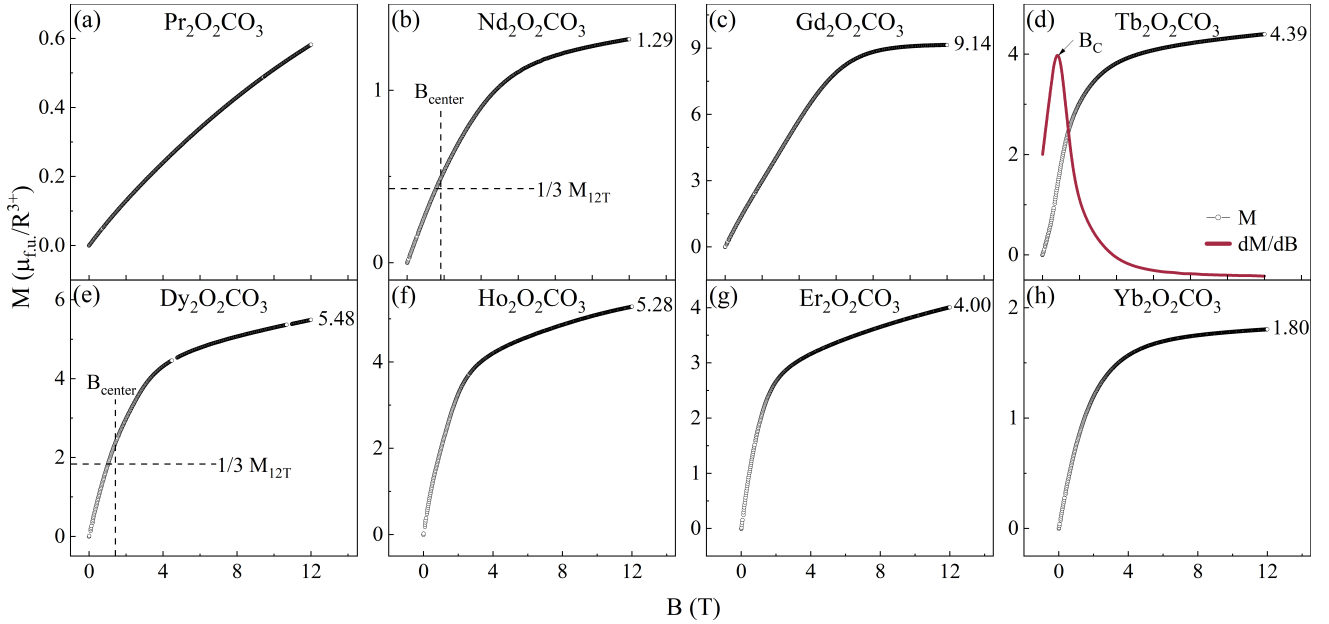


FIG. 5. DC magnetization curves measured at 2 K from 0 to 12 T for $\text{RE}_2\text{O}_2\text{CO}_3$. The estimated saturation values, $M_{12\text{T}}$, are labeled at the end of each curve besides the Pr sample. The derivative of $\text{Tb}_2\text{O}_2\text{CO}_3$ is plotted in red. The curves of $\text{Nd}_2\text{O}_2\text{CO}_3$ and $\text{Dy}_2\text{O}_2\text{CO}_3$ include demarcations of one-third of the $M_{12\text{T}}$ value and B_{center} from $\chi'(B)$ data.

The description of the DC magnetic properties and AC susceptibility data for each sample is listed below.

A. $\text{Pr}_2\text{O}_2\text{CO}_3$

For $\text{Pr}_2\text{O}_2\text{CO}_3$, the high temperature CW fit of $1/\chi$ (Fig. 4(a)) yields a $\theta_{\text{CW}} = -49.71$ K and a $\mu_{\text{eff}} = 3.48 \mu_{\text{B}}$. This μ_{eff} value is consistent with the free-ion moment of $\mu_{\text{eff}}^{\text{theo}} = 3.58 \mu_{\text{B}}$ expected for Pr^{3+} ions. $1/\chi$ shows a weak slope change below 50 K, suggesting changes of magnetic

moments and spin-spin interactions in these temperature regions due to CEF effects. The low temperature CW fit yields a $\theta_{CW} = -37.32$ K and a $\mu_{\text{eff}} = 3.62 \mu_B$. Such large θ_{CW} does not necessarily reflect the intrinsic strength of the magnetic exchange interaction of $\text{Pr}_2\text{O}_2\text{CO}_3$, but could be related to the competition between the exchange interaction and the split between the ground-state doublet of Pr^{3+} ions (see details in the Discussion). In fact, our AC susceptibility measurement shows weak and noisy signals (not plotted here), which suggests a nonmagnetic ground state.

B. $\text{Nd}_2\text{O}_2\text{CO}_3$

For $\text{Nd}_2\text{O}_2\text{CO}_3$, the high temperature CW fit of $1/\chi$ (Fig. 4(b)) yields a $\theta_{CW} = -48.51$ K and a $\mu_{\text{eff}} = 3.79 \mu_B$. This μ_{eff} value is consistent with the free-ion moment of $\mu_{\text{eff}}^{\text{theo}} = 3.62 \mu_B$ expected for Nd^{3+} ions. The low temperature CW fit yields a $\theta_{CW} = -4.13$ K and a $\mu_{\text{eff}} = 2.66 \mu_B$.

For $\text{Nd}_2\text{O}_2\text{CO}_3$, a fast drop of its AC susceptibility (Fig. 6(a)), $\chi'(T)$, or a sharp peak of $d\chi'/dT$, occurs around 1.37 K, following a broad peak around 1.5 K. Such a feature suggests emerging long range magnetic order at $T_N = 1.37$ K. With increasing DC magnetic field, the position of the fast drop shifts towards lower temperatures and the peak becomes even broader. Meanwhile, the DC field scan of $\chi'(B)$ (Fig. 6(c)) measured at base temperature $T = 0.34$ K shows two peaks at $B_{C1} = 1.04$ T and $B_{C2} = 2.75$ T and then becomes flat around $B_S = 5.7$ T. In principal, $\chi'(B)$ measures the derivative of the DC magnetization $M(B)$, therefore the peaks of $\chi'(B)$ suggest the existence of field induced spin state transitions and the flatness at high field suggests the emergence of a spin-polarized state. Accordingly, B_S is the saturation field. With increasing temperature, these two peak positions of B_{C1} and B_{C2} exhibit little change. Using the critical temperatures and critical fields, a magnetic phase diagram was constructed in Fig. 6(d).

C. $\text{Gd}_2\text{O}_2\text{CO}_3$

For $\text{Gd}_2\text{O}_2\text{CO}_3$, the CW fit of $1/\chi$ from 150 to 300 K (Fig. 4(c)) yields a $\theta_{CW} = -5.42$ K and a $\mu_{\text{eff}} = 8.97 \mu_B$. This μ_{eff} value is consistent with the free-ion moment of $\mu_{\text{eff}}^{\text{theo}} = 7.94 \mu_B$ expected for Gd^{3+} ions. The $\chi'(T)$ (Fig. 7(a)) shows a drop, or a peak of $d\chi'/dT$, around $T_N = 1.26$ K, which suggests long range magnetic ordering. With increasing DC magnetic field, this feature becomes weaker and a broad peak develops. The $\chi'(B)$ data (Fig. 7(c)) suggests a saturation field around 1.6 T.

D. $\text{Tb}_2\text{O}_2\text{CO}_3$

For $\text{Tb}_2\text{O}_2\text{CO}_3$, the high temperature CW fit of $1/\chi$ (Fig. 4(d)) yields a $\theta_{CW} = -9.06$ K and a $\mu_{\text{eff}} = 9.52 \mu_B$. This μ_{eff} value is consistent with the free-ion moment of $\mu_{\text{eff}}^{\text{theo}} = 9.72 \mu_B$ expected for Tb^{3+} ions. The low temperature CW fit yields a $\theta_{CW} = -6.70$ K and a $\mu_{\text{eff}} = 8.85 \mu_B$.

For $\text{Tb}_2\text{O}_2\text{CO}_3$, the $\chi'(T)$ (Fig. 8(a)) shows a drop, or a peak of $d\chi'/dT$, around 2.10 K, following a broad peak around 2.8 K. This suggests long range magnetic ordering at $T_N = 2.10$ K. With increasing DC magnetic field, this features shifts towards lower temperatures. The $\chi'(B)$ data (Fig. 8(b)) measured at base temperature $T = 0.46$ K shows a peak at $B_C = 0.90$ T and becomes flat around $B_S = 5.3$ T. Correspondingly, the derivative of DC magnetization, $M(B)$, measured at 2.0 K also shows a peak at $B_C = 0.8$ T, as plotted in Fig. 5(d). With increasing temperature, this peak position remains relatively the same. A magnetic phase diagram was constructed in Fig. 8(c).

E. $\text{Dy}_2\text{O}_2\text{CO}_3$

For $\text{Dy}_2\text{O}_2\text{CO}_3$, the high temperature CW fit of $1/\chi$ (Fig. 4(e)) yields a $\theta_{CW} = -1.30$ K and a $\mu_{\text{eff}} = 10.20 \mu_B$. This μ_{eff} value is consistent with the free-ion moment of $\mu_{\text{eff}}^{\text{theo}} = 10.65 \mu_B$ expected for Dy^{3+} ions. The low temperature CW fit yields a $\theta_{CW} = -8.70$ K and a $\mu_{\text{eff}} = 9.33 \mu_B$.

For $\text{Dy}_2\text{O}_2\text{CO}_3$, a fast drop of $\chi'(T)$ (Fig. 9(a)), or a sharp peak of $d\chi'/dT$, occurs around 1.70 K, following a broad peak around 2.0 K. This suggests long range magnetic ordering at $T_N = 1.70$ K. With increasing DC magnetic field, the fast drop position shifts to lower temperatures and peak becomes even broader. Meanwhile, $\chi'(B)$ (Fig. 9(b)) measured at base temperature $T = 0.34$ K shows two peaks at $B_{C1} = 0.70$ T and $B_{C2} = 2.32$ T, and then becomes flat around $B_S = 9$ T (not shown here). With increasing temperature, these two peak positions change little, until $T = 1.55$ K, wherein the peaks significantly broaden and shift toward lower fields. Its magnetic phase diagram was constructed in Fig. 9(c).

F. $\text{Ho}_2\text{O}_2\text{CO}_3$

For $\text{Ho}_2\text{O}_2\text{CO}_3$, the high temperature CW fit of $1/\chi$ (Fig. 5(f)) yields a $\theta_{CW} = -0.19$ K and a $\mu_{\text{eff}} = 9.67 \mu_B$. This μ_{eff} value is consistent with the free-ion moment of $\mu_{\text{eff}}^{\text{theo}} = 10.61 \mu_B$ expected for Ho^{3+} ions. The low temperature CW fit yields a $\theta_{CW} = -6.83$ K and a $\mu_{\text{eff}} = 9.41 \mu_B$.

$\chi'(T)$ (Fig. 10(a,b)) shows a drop, or a peak of $d\chi'/dT$, around 0.73 K, following a broad peak around 1.2 K. This suggests long range magnetic ordering at $T_N = 0.73$ K. With increasing DC magnetic field, these fea-

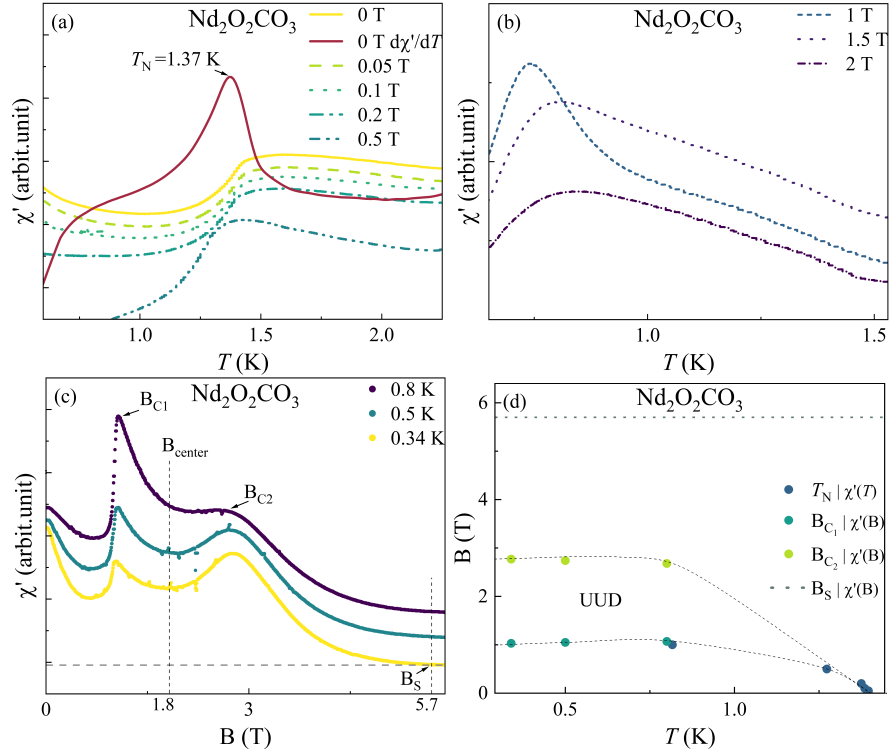


FIG. 6. $\text{Nd}_2\text{O}_2\text{CO}_3$ (a): Temperature dependence of χ' measured at various low DC fields. The derivative of 0 T data is marked in red. (b): Temperature dependence of χ' at DC fields 1–2 T. (c): DC field dependence of χ' at low temperatures. (d): Magnetic phase diagram. The possible UUD phase is labeled.

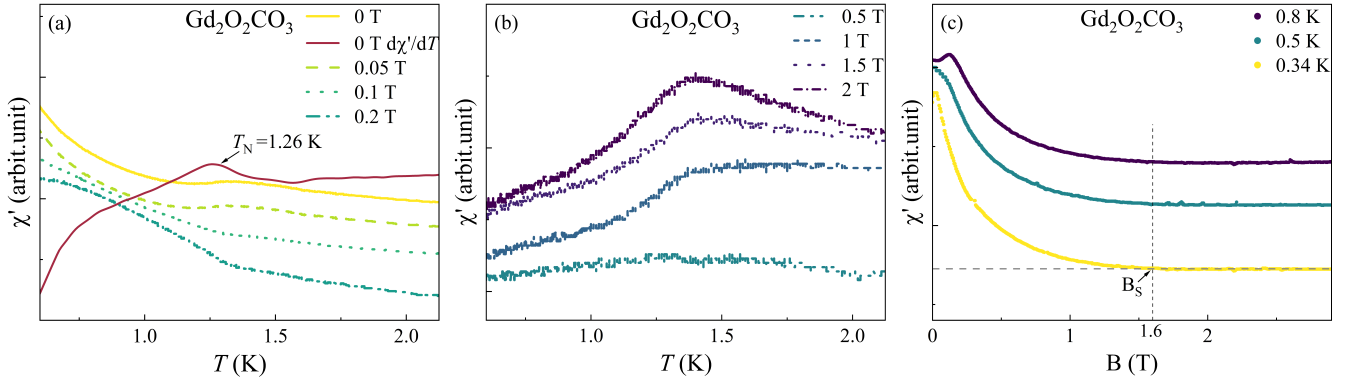


FIG. 7. $\text{Gd}_2\text{O}_2\text{CO}_3$ (a): Temperature dependence of χ' measured at various low DC fields. The derivative of 0 T data is marked in red. (b): Temperature dependence of χ' at higher DC fields. (c): DC field dependence of χ' at low temperatures.

tures shift to low temperatures. The $\chi'(B)$ data (Fig. 10(c)) measured at base temperature $T = 0.34$ K shows a single peak at $B_C = 1.40$ T and becomes flat around $B_S = 5.5$ T (not shown here). With increasing temperature, the peak position changes little. Its magnetic phase diagram was constructed Fig. 10(d).

G. $\text{Er}_2\text{O}_2\text{CO}_3$

For $\text{Er}_2\text{O}_2\text{CO}_3$, the high temperature CW fit of $1/\chi$ (Fig. 4(g)) yields a $\theta_{\text{CW}} = -2.94$ K and a $\mu_{\text{eff}} = 7.85$

μ_B . This μ_{eff} value is slightly smaller than the free-ion moment of $\mu_{\text{eff}}^{\text{theo}} = 9.58 \mu_B$ expected for Er^{3+} ions. The low temperature CW fit yields a $\theta_{\text{CW}} = -4.00$ K and a $\mu_{\text{eff}} = 7.35 \mu_B$.

For $\text{Er}_2\text{O}_2\text{CO}_3$, the $\chi'(T)$ (Fig. 11(a)) shows a peak around $T_N = 1.58$ K, suggesting the occurrence of a long range magnetic ordering. With increasing DC magnetic field, this feature shifts to low temperatures. The $\chi'(B)$ data (Fig. 11(b)) measured at base temperature $T = 0.46$ K shows a peak at $B_C = 0.76$ T and becomes flat around $B_S = 3.0$ T (not shown here). With increasing temperature, the peak position does not change too much

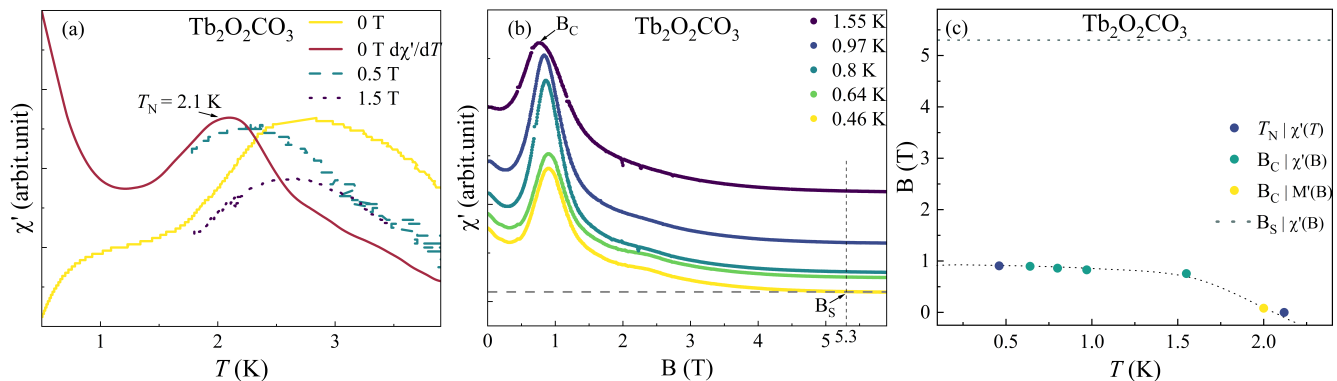


FIG. 8. $\text{Tb}_2\text{O}_2\text{CO}_3$ (a): Temperature dependence of χ' measured at various DC fields. The derivative of 0 T data is marked in red. (b): DC field dependence of χ' at low temperatures. (c): Magnetic phase diagram.

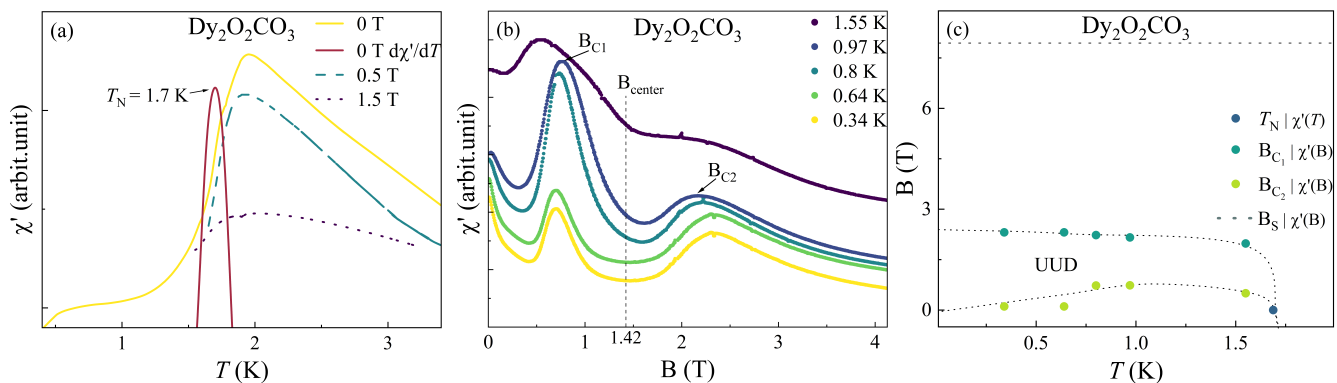


FIG. 9. $\text{Dy}_2\text{O}_2\text{CO}_3$ (a): Temperature dependence of χ' measured at various DC fields. The derivative of 0 T data is marked in red. (b): DC field dependence of χ' at low temperatures. (c): Magnetic phase diagram. The possible UUD phase is labeled.

but the peak becomes weaker and disappears above 1.55 K. Its magnetic phase diagram was constructed in Fig. 11(c).

NPD measurements of the Er sample were also performed to study its magnetic structure. The NPD pattern measured at 20 K confirms its hexagonal lattice structure with space group $P6_3/mmc$ (Fig. 1(a)). The lattice parameters were determined to be $a = b = 3.823$ (1) Å and $c = 15.044$ (2) Å, which are consistent with XRD results (Table I). The NPD pattern measured at 0.3 K showed 3 main magnetic peaks (Fig. 12(b)). Based on them, the propagation vector was resolved to be $(\frac{1}{3}, \frac{1}{3}, 0.41)$, indicating incommensurate magnetic ordering. While the exact magnetic structure was unsolvable due to the number of parameters in the refinement—resulting from the four independent magnetic ions in each unit cell—attempts to refine the data were made by introducing several extra constraints.

Using the FULLPROF software, a spiral model was used to represent the spins in the refinement. As shown in Fig. 13(a), each spin (green arrow) in a unit cell can be described by three angles. θ and ϕ represent the orientation of the rotation axis, and ψ describes the angle between the spin and the rotation axis. A relative phase factor also needs to be included to determine the

orientation of the spin. Thereafter, the spins in all the other unit cells can be generated by rotating the spins around rotation axes according to the propagation vector. To refine the experimental data, several constraints were included by using this spiral model. For the four spins in each unit cell, we assumed (i) all of them have the same magnetic moment and same rotation axis and (ii) the ψ angle is 90 degrees. It is obvious that, under these constraints, all spins lie in the plane perpendicular to the rotation axis. Accordingly, the refinement shows that the θ angle was resolved to be around 90 degrees, which means the rotation axis lies in the ab -plane. The goodness of fitting appeared unaffected by the value of ϕ . To confirm this, the whole (θ, ϕ) space with a 2 degree step size was surveyed and constructed a (R, θ, ϕ) contour plot constructed (Fig. 14). The sphere was mapped to a disk using the Lambert azimuthal equal-area projection. From the plot, it is confirmed that the fit is optimized as long as θ is near 90 degrees. This a reasonable result due to the isotropy in the triangular lattice (ab -plane).

Based on all these considerations, refinement of the 0.3 K NPD data leads to a spiral spin structure, as shown in Fig. 12(b) and (c). Several features are (i) the magnetic moment of each spin is $4.21(2) \mu_B$; (ii) the rotation axis can be any orientation within the ab -plane—it

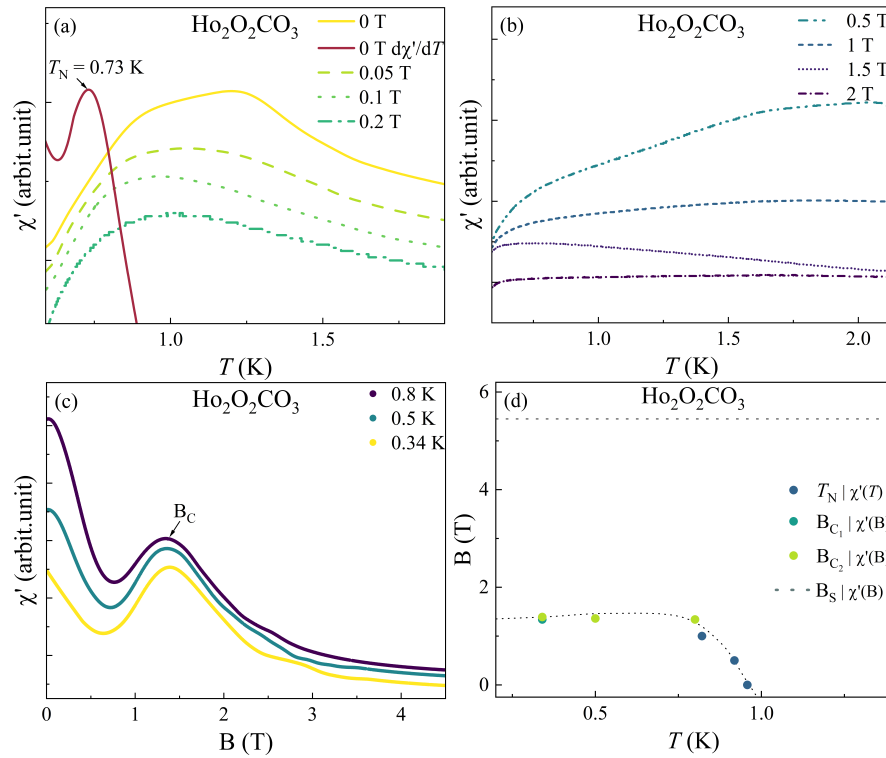


FIG. 10. $\text{Ho}_2\text{O}_2\text{CO}_3$ (a): Temperature dependence of χ' measured at various low DC fields. The derivative of 0 T data is marked in red. (b): Temperature dependence of χ' at DC fields 0.5–2 T. (c): DC field dependence of χ' at low temperatures. (d): Magnetic phase diagram.

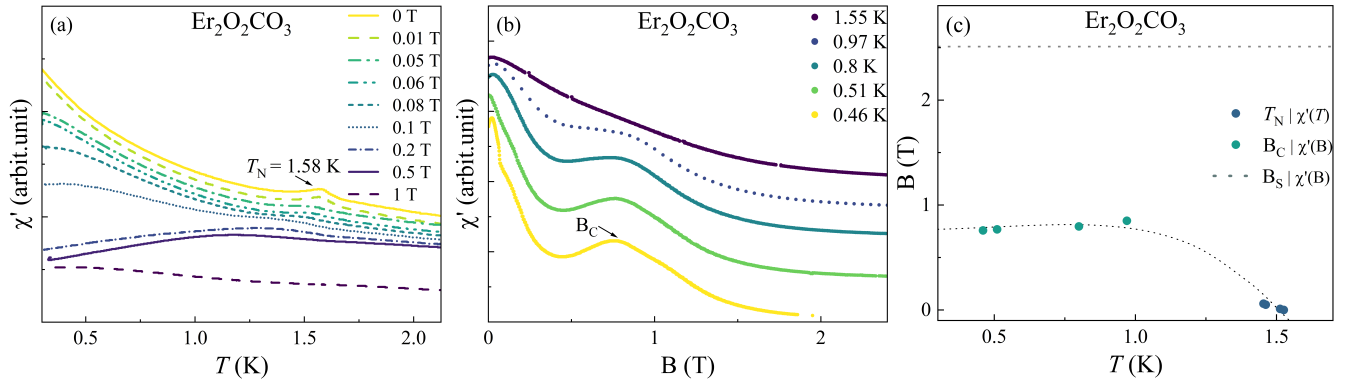


FIG. 11. $\text{Er}_2\text{O}_2\text{CO}_3$ (a): Temperature dependence of χ' measured at various DC fields. (b): DC field dependence of χ' at low temperatures. (c): Magnetic phase diagram.

was chosen to be the b -axis in Fig.13 for convenience. (iii) the k_x, k_y are both $1/3$, suggesting a 120-degree spin structure in the triangular layer (ab -plane); (iv) along the c -axis, each spin in the unit cell forms a cycloid structure with the rotation angle to be $k_z * 360 = 147.6$ degrees (Fig. 13(c)); (v) the two spins in each bilayer (highlighted by the dashed rectangle in Fig. 13(b) and (c)) have inversion symmetry relations (from (x,y,z) to $(-x,-y,-z)$), which requests them to have opposite propagation vectors (k and $-k$) in an incommensurate ordering state. Therefore, these two spins rotate in opposite directions while the angle between them varies in differ-

ent bilayers; meanwhile, (vi) the inter-bilayer spins share the same propagation vector and that are roughly ferromagnetically aligned. This fit, while imperfect, captures the main features of the NPD pattern. The difference of the magnetic peak intensities between the data and our calculation may originate from the extra constraints we included and the possible diffuse scattering as suggested by the broadening of the magnetic peaks.

This proposed spin structure was also confirmed to be reasonable by representative analysis. In the space group $P6_3/mmc$ with the propagation vector $\mathbf{k} = (.33333, .33333, .42319)$, the decomposition of the mag-

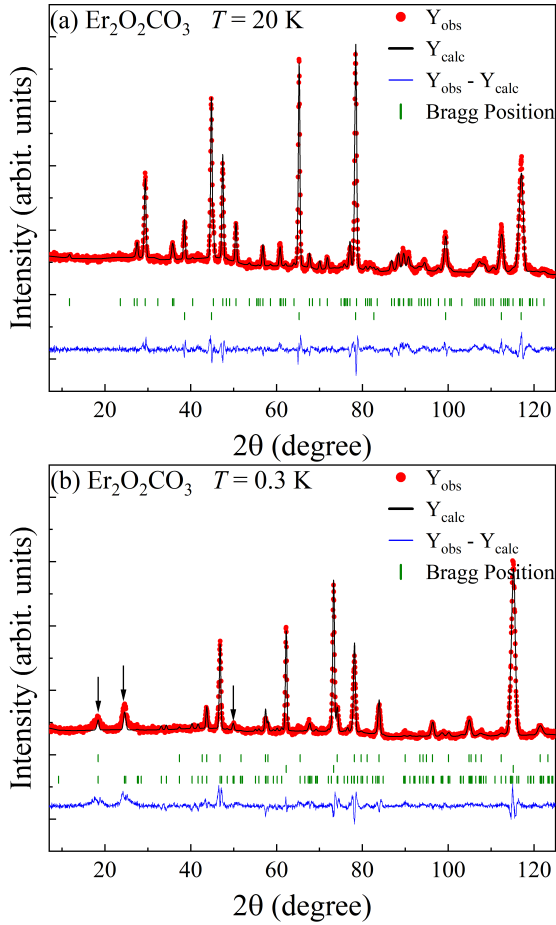


FIG. 12. NPD data for $\text{Er}_2\text{O}_2\text{CO}_3$. (a): The NPD pattern measured at 20 K with a neutron wavelength of 1.54\AA (red) and its Rietveld refinement. Green bars show the positions of nuclear Bragg peaks for $\text{Er}_2\text{O}_2\text{CO}_3$ (top) and the aluminum can (bottom) which held the sample during measurements. (b): The NPD data measured at 0.3 K with a neutron wavelength of 2.41\AA and its Rietveld refinement. The green bars show the positions of nuclear Bragg peaks of $\text{Er}_2\text{O}_2\text{CO}_3$ (top), Al can (middle), and magnetic Bragg peaks of $\text{Er}_2\text{O}_2\text{CO}_3$ (bottom). Black arrows highlight the main magnetic Bragg peaks.

netic representation for all the Er sites are $\Gamma_{\text{mag}} = 1\Gamma_1^1 + 1\Gamma_2^1 + 2\Gamma_3^2$. And the basis vectors of Γ_3 irreducible representative can best describe this spin structure.

H. $\text{Yb}_2\text{O}_2\text{CO}_3$

For $\text{Yb}_2\text{O}_2\text{CO}_3$, The high temperature CW fit of χ (Fig. 4(h)) yields a $\theta_{\text{CW}} = -44.25$ K and a $\mu_{\text{eff}} = 4.39 \mu_{\text{B}}$. This μ_{eff} value is slightly smaller than the free-ion moment of $\mu_{\text{eff}}^{\text{theo}} = 4.54 \mu_{\text{B}}$ expected for Yb^{3+} ions. The low temperature CW fit yields a $\theta_{\text{CW}} = -0.94$ K and a $\mu_{\text{eff}} = 3.25 \mu_{\text{B}}$.

$\chi'(T)$ (Fig. 15(a, b)) shows no sharp feature but a broad peak around 0.6 K. With increasing DC magnetic

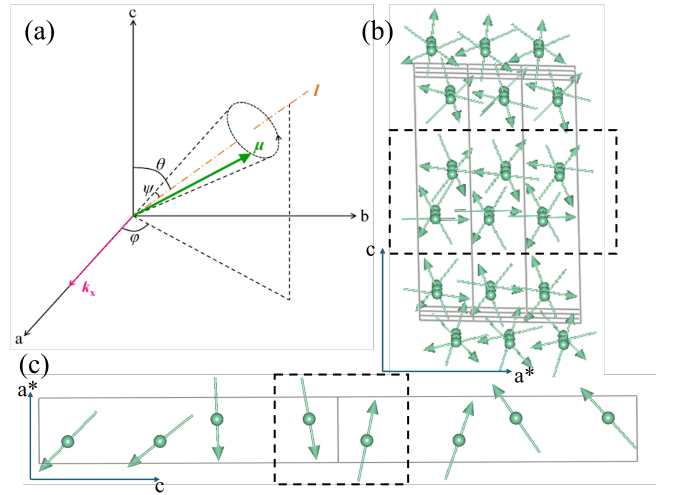


FIG. 13. (a): A representation of spin as illustrated by the spiral model in the EDPCR software of the FULLPROF package. (b): A tentative spin structure of $\text{Er}_2\text{O}_2\text{CO}_3$ in its magnetic ordering state. All spins lie in the ac -plane and form a 120-degree spin structure in the triangular plane (ab -plane). (c): Meanwhile, each spin in a unit cell and its corresponding spins in other unit cells form a cycloid structure along the c -axis. The black dashed rectangles highlight the bilayer triangular structure.

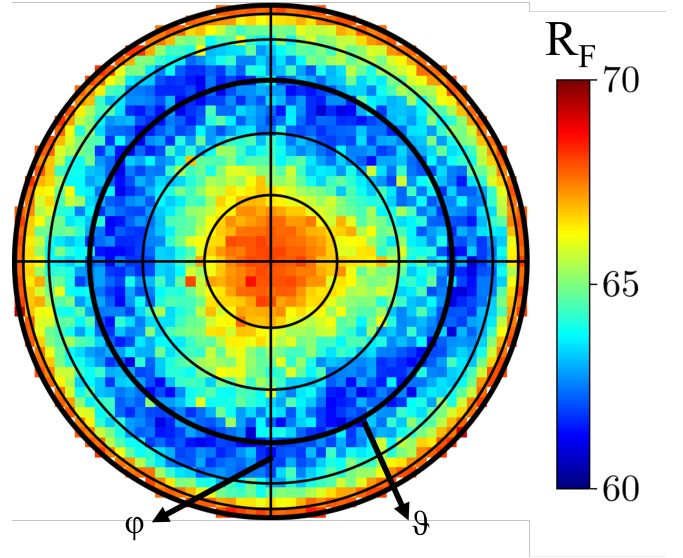


FIG. 14. A contour plot representing the relationship between the R_F factor of fitting and the direction of the rotation axis in the spiral model. The spherical coordinates are mapped to polar coordinates by using Lambert azimuthal equal-area projection.

field, this broad peak shifts to low temperatures. For example, it shifts to 0.2 K with $B = 0.1$ T (Fig. 15(b)). The $\chi'(B)$ data (Fig. 15(c)) measured at $T = 0.46$ K becomes flat around $B_S = 1.5$ T. As shown in Fig. 15(d), this broad peak shows no obvious frequency dependence

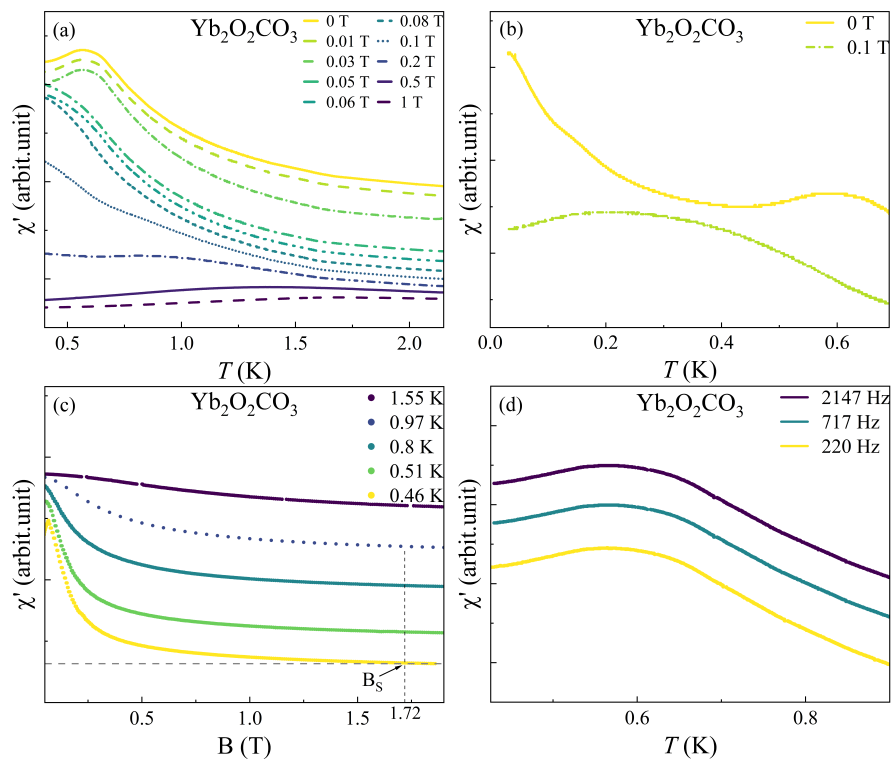


FIG. 15. $\text{Yb}_2\text{O}_2\text{CO}_3$ (a): Temperature dependence of χ' measured at various DC fields.. (b): Low temperature regime—down to 50 mK—for zero and 0.1 T data. (c): DC field dependence of χ' at various temperatures. (d): Temperature dependence of χ' with different AC field frequencies.

between 220 Hz and 2147 Hz. Such a broad peak without sharp features suggests that short range magnetic ordering develops around 0.6 K for $\text{Yb}_2\text{O}_2\text{CO}_3$ yet no long range ordering appears down to 0.03 K, the lowest temperature measured (Fig. 15(b)). The independence of frequency further suggests this short range ordering is not glass-like.

V. DISCUSSION

All $\text{RE}_2\text{O}_2\text{CO}_3$ members show antiferromagnetic exchange interactions as shown by the negative θ_{CW} obtained by low temperature CW fit. Meanwhile, various magnetic ground states were observed, including (i) a nonmagnetic ground state for the Pr sample; (ii) long range magnetic ordering states for the Nd, Gd, Tb, Dy, Ho, and Er samples; and, (iii) a short range ordering state for the Yb sample. Some general magnetic properties among the long range ordered samples are: (i) for the Nd, Gd, Tb, Dy, and Ho samples, the zero field of $\chi'(T)$ exhibits a broad peak followed by a fast drop, which represents the development of short range ordering correlations and thereafter the occurrence of a long range magnetic ordering, respectively. Such behavior is typical for low dimensional antiferromagnets. (ii) For the Nd, Tb, Dy, Ho, and Er samples, the $\chi'(B)$ data exhibits one or two peaks, which suggests field induced spin state

transitions.

We can categorize the eight $\text{RE}_2\text{O}_2\text{CO}_3$ samples by two groups. Five of them ($\text{RE} = \text{Nd, Gd, Dy, Er, Yb}$) have Kramers ions, whose single-ion ground state doublet is restrictively protected by time-reversal symmetry, and are thus degenerate in energy for a mean field of zero. Therefore, their low temperature magnetism can be described by an effective moment $J_{\text{eff}} = 1/2$. Among them, Gd^{3+} is special due to its half-filled $4f$ shell ($4f^7$, $S = 7/2$, $L = 0$) with Heisenberg-like anisotropy and effective moment $S_{\text{eff}} = 7/2$. The remaining three ($\text{RE} = \text{Pr, Tb, Ho}$) have non-Kramers ions, whose single-ion ground state could also be a doublet but not necessarily degenerate.

If the degeneracy of the non-Kramers doublet is naturally removed due to the local environment of the RE^{3+} ions, which splits the doublet into two nonmagnetic singlet states with a finite energy difference, two scenarios can occur. First, if the spin-spin interactions (exchange/dipolar interactions) is comparable to the energy splitting of the two lowest singlet states, the spin-spin interactions can act as local exchange fields to mix the two nearby singlet states and recover the magnetic moment. Accordingly, the low temperature magnetism of such a system could be treated with an effective pseudospin $S_{\text{eff}} = 1/2$. On the other hand, if the two lowest singlet states get too separated in energy, the spin-spin interactions will be insufficient to induce magnetism and thus a non-

TABLE III. Magnetic ordering temperature and calculated exchange interaction (J_{nn}), dipolar interaction (D), and effective exchange interaction (J_{ex}) for $\text{RE}_2\text{O}_2\text{CO}_3$

Compound	f Orbitals (RE^{3+})	Ordering Temperature T_{N} (K)	J_{ex} (K)	D (K)	J_{nn} (K)
$\text{Pr}_2\text{O}_2\text{CO}_3$	$4f^2$	—	—	—	—
$\text{Nd}_2\text{O}_2\text{CO}_3$	$4f^3$	1.37	-2.75	0.07	-2.82
$\text{Gd}_2\text{O}_2\text{CO}_3$	$4f^7$	1.26	-3.61	0.84	-4.45
$\text{Tb}_2\text{O}_2\text{CO}_3$	$4f^8$	2.10	-4.46	0.83	-5.29
$\text{Dy}_2\text{O}_2\text{CO}_3$	$4f^9$	1.70	-5.80	0.94	-6.74
$\text{Ho}_2\text{O}_2\text{CO}_3$	$4f^{10}$	0.73	-4.56	0.97	-5.53
$\text{Er}_2\text{O}_2\text{CO}_3$	$4f^{11}$	1.58	-2.67	0.60	-3.27
$\text{Yb}_2\text{O}_2\text{CO}_3$	$4f^{13}$	—	-0.63	0.12	-0.75

magnetic ground state is expected. Accordingly, the Tb and Ho samples with long range magnetic ordering belong to the first scenario and the Pr sample with a non-magnetic ground state belongs to the second. Recently, several other Pr-compounds $\text{Pr}_3\text{A}_2\text{Sb}_3\text{O}_{14}$ (A = Mg and Zn) [87, 88] with a Pr^{3+} kagome lattice and Pr_3BWO_9 [89] with a distorted Pr^{3+} kagome lattice have also been reported to exhibit a nonmagnetic ground state.

Indeed, the low temperature magnetic properties of the Nd, Tb, Dy, Ho, Er, and Yb samples, such as that the obtained low temperature μ_{eff} is smaller than the free-ion moment and that the measured magnetization at 2 K saturates at a value smaller than the expected free-ion saturation value, reflect the nature of effective spin- $1/2$ moment.

The effective exchange interaction (J_{ex}) between the nearest neighbor RE^{3+} ions on a triangular lattice can be approximately calculated as $J_{\text{ex}} = 3k_{\text{B}}\theta_{\text{CW}}/zS(S+1)$, where we use $S = 1/2$ due to the effective spin- $1/2$ moment and $z = 6$ as the number of nearest-neighbor spins. Here, we neglect the two kinds of inter-layer interactions along the c -axis. One is the interaction between the adjacent two bilayers, which should be small due to the large distance and the blockage of carbonate group between them. The other is the interaction within each bilayer, which again should be small since the relative shift of the RE^{3+} ions between two triangular layers within each bilayer leads to a frustrated inter-layer magnetic coupling. Meanwhile, the dipolar interaction can be estimated by $D = \mu_0\mu_{\text{eff}}^2/4\pi R_{\text{nn}}^3$, where R_{nn} is the nearest neighbor distance of RE^{3+} ions on a triangular layer. Since the effective exchange interaction $J_{\text{ex}} = J_{\text{nn}} + D$, in which J_{nn} is the magnetic superexchange interaction between the nearest neighbor RE^{3+} ions, we calculated the J_{nn} value as listed in Table III.

It is interesting to observe only short range ordering but no long range ordering down to 0.03 K for $\text{Yb}_2\text{O}_2\text{CO}_3$, which makes it another possible QSL candidate with $J_{\text{eff}} = 1/2$ Yb^{3+} -triangular lattice. To com-

pare it with other reported Yb-TLAF QSL candidates, their θ_{CW} and μ_{eff} obtained from the low temperature CW fit and nearest-neighbor distance of Yb^{3+} ions are listed in Table IV. While the strength of the exchange interaction represented by the θ_{CW} does not simply depend on the nearest neighbor distance but also the exchange path which varies in different systems, one general trend is that the θ_{CW} notably decreases after the nearest neighbor distance exceeds 5 Å. Such a small exchange interaction makes them not ideal systems to explore exchange interaction based QSL state. For $\text{Yb}_2\text{O}_2\text{CO}_3$, a $\theta_{\text{CW}} = -0.94$ K represents a moderate strong exchange interaction compared to the others, which makes it possible to study a QSL state below the Kelvin energy level. As mentioned above, the disrupted inter-layer interaction within the bilayer could be the main obstacle of long range ordering in $\text{Yb}_2\text{O}_2\text{CO}_3$. A similar example is the 6HB- $\text{Ba}_3\text{NiSb}_2\text{O}_9$ with Ni^{2+} -triangular lattice, in which the adjacent Ni^{2+} layers have the same shift as those of $\text{Yb}_2\text{O}_2\text{CO}_3$ [90, 91]. 6HB- $\text{Ba}_3\text{NiSb}_2\text{O}_9$ also exhibits no magnetic ordering down to at least 0.3 K and has been studied as a rare spin-1 QSL candidate. Meanwhile, 6HA- $\text{Ba}_3\text{NiSb}_2\text{O}_9$, another phase of $\text{Ba}_3\text{NiSb}_2\text{O}_9$ with the Ni^{2+} -triangular layers arranged exactly on top of one another, displays long range magnetic ordering at 13.5 K, for which the inter-layer coupling plays an important role [90, 92, 93]. Both $\text{Yb}_2\text{O}_2\text{CO}_3$ and 6HB- $\text{Ba}_3\text{NiSb}_2\text{O}_9$ demonstrate that TLAFs with shifted triangular layer arrangements can be a good platform for exploring QSL candidates.

Finally, the magnetic phase diagrams of the Nd and Dy samples show a series of field-induced spin state transitions. When a magnetic field is applied along the easy-axis or within the easy-plane of a TLAF, a spin up-up-down (UUD) phase could be stabilized within a regime of the field to exhibit a $1/3$ M_{s} magnetization plateau. Such a plateau has been observed in single crystals of TLAFs $\text{Ba}_3\text{CoSb}_2\text{O}_9$ [94–100], $\text{Na}_2\text{BaA}(\text{PO}_4)_2$ (A = Co, Ni, Mn) [101–105], and AYbSe_2 (A = Na, K, Cs) [22, 31, 106].

TABLE IV. Table of Yb-TLAF QSL candidates with their θ_{CW} and μ_{eff} obtained from the low temperature CW fit and nearest-neighbor distance of Yb^{3+} ions. Parentheticals include magnetic field orientations, with (\perp) and (\parallel) identifying field applied perpendicular and parallel to the ab -plane, respectively.

Compound	Low T θ_{CW} (K)	Low T μ_{eff} (μ_{B})	Nearest-Neighbor Distance (\AA)	Reference
NaYbO_2	-5.64	2.84	3.34	[15]
$\text{YbZn}_2\text{GaO}_5$	-5.22 (\perp)	4.36*	3.37	[43]
	-3.77 (\parallel)	—		
YbMgGaO_4	-4.11	2.8	3.4	[38, 39] [†]
YbBO_3	-0.8	3.2	3.75	[34]
$\text{Yb}_2\text{O}_2\text{CO}_3$	-0.94	3.25	3.77	This work.
NaYbS_2	-13.5 (\perp)	3.2 (\perp)	~ 3.90	[19]
	-4.5 (\parallel)	1.8 (\parallel)		
NaYbSe_2	~ -7	2.43	4.06	[22]
CsYbSe_2	-22.6 (\perp)	3.21 (\perp)	4.15	[49]
	-13.2 (\parallel)	3.48 (\parallel)		
$\text{NaBaYb}(\text{BO}_3)_2$	-0.069	2.23	5.33	[53] [§]
$\text{KBaYb}(\text{BO}_3)_2$	-0.84	2.67	5.42	[54]
$\text{K}_3\text{Yb}(\text{VO}_4)_2$	~ -1	2.41	5.85	[44]
$\text{Ba}_6\text{Yb}_2\text{Ti}_4\text{O}_{17}$	-0.49	2.5	5.91	[46]
$\text{Ba}_3\text{Yb}(\text{BO}_3)_3$	-0.077	2.31	7.18	[113]

* Effective moment from high temperature range, 200–300 K.

[†] Taken from temperatures $\gtrsim 8$ K.

[§] Values averaged from magnetic fields applied perpendicular and parallel to the c -axis.

Typically, the $dM(B)/dB$ or $\chi'(B)$ data shows two sharp peaks at the critical field positions and a deep valley between them for the UUD phase. For polycrystalline sam-

ples, these features become a shallow valley within two broad peaks due to the powder averaging effect, which have been observed in $\text{A}_3\text{CoB}_2\text{O}_9$ ($A = \text{Ba}, \text{Sr}$ and $B = \text{Nb}, \text{Ta}$) [107–110] and $\text{Ba}_2\text{La}_2\text{ATe}_2\text{O}_{12}$ ($A = \text{Co}, \text{Ni}$) [111, 112]. A similar phenomena in $\chi'(B)$ was observed for our polycrystalline Nd and Dy samples, which suggests a field induced UUD phase between the two critical fields (Fig. 6(d) and Fig. 9(c)). Indeed, the magnetization value at $B_{\text{center}} = 1.82$ T for Nd and $B_{\text{center}} = 1.42$ T for Dy are $0.49 \mu_{\text{B}}/\text{Nd}^{3+}$ and $2.37 \mu_{\text{B}}/\text{Dy}^{3+}$ respectively, which are roughly $\frac{1}{3}$ of their $M_{12\text{T}}$ value, as shown in Fig. 5(b),(e). Here B_{center} is the field position at the center of the valley of $\chi'(B)$ data, as labeled in Fig. 6(c) and Fig. 9(b).

VI. CONCLUSION

In summary, most of the $\text{RE}_2\text{O}_2\text{CO}_3$ ($\text{RE} = \text{Nd}, \text{Gd}, \text{Tb}, \text{Dy}, \text{Ho}, \text{Er}$), either Kramers ions or non Kramers ions, exhibit long range magnetic ordering and field induced spin state transition at low temperatures. Two anomalies are Pr and Yb samples. For Pr sample, its nonmagnetic ground state could be due to the larger gap between the splitting non Kramers ground doublet compared to its spin spin interactions. For Yb sample, the shift between the Yb^{3+} ions on adjacent triangular layers within the bilayer causes the frustrated inter-layer interaction and prevents its long range magnetic ordering. This makes $\text{Yb}_2\text{O}_2\text{CO}_3$ a good candidate for QSL studies, joining a good number of other Yb^{3+} -TLAFs that have been studied as QSL candidates. Certainly, $\text{RE}_2\text{O}_2\text{CO}_3$ is a new family of RE-TLAFs exhibiting interesting magnetic properties and deserves future studies.

ACKNOWLEDGMENTS

Research at the University of Tennessee is supported by the Air Force Office of Scientific Research under grant no. FA9550-23-1-0502. A portion of this work was performed at the National High Magnetic Field Laboratory, which is supported by National Science Foundation Cooperative Agreement No. DMR-1644779 and the State of Florida.

-
- [1] P. W. Anderson, Resonating valence bonds: A new kind of insulator?, *Materials Research Bulletin* **8**, 153 (1973).
 - [2] A. P. Ramirez, Geometrical frustration in magnetism, *Czechoslovak Journal of Physics* **46**, 3247 (1996).
 - [3] M. Collins and O. Petrenko, Triangular antiferromagnets, *Can. J. Phys.* **75**, 605 (1997).
 - [4] A. Harrison, First catch your hare: the design and synthesis of frustrated magnets, *J. Phys.: Condens. Matter* **16**, S553 (2004).
 - [5] L. Balents, Spin liquids in frustrated magnets, *Nature* **464**, 199 (2010).
 - [6] T. Moriya, New mechanism of anisotropic superexchange interaction, *Physical Review Letters* **4**, 228 (1960).
 - [7] U. Arjun, K. Brinda, M. Padmanabhan, and R. Nath, Magnetic properties of layered rare-earth oxycarbonates $\text{Ln}_2\text{O}_2\text{CO}_3$ ($\text{Ln}=\text{Nd}, \text{Sm}, \text{and Dy}$), *Solid State Communications* **240**, 1 (2016).
 - [8] Y. Zhou, K. Kanoda, and T.-K. Ng, Quantum spin liquid states, *Review of Modern Physics* **89**, 025003 (2017).
 - [9] L. Savary and L. Balents, Quantum spin liquids: a review, *Reports on Progress in Physics* **80**, 016502 (2017).

- [10] Y. Li *et al.*, Spin liquids in geometrically perfect triangular antiferromagnets, *Journal of Physics: Condensed Matter* **32**, 224004 (2020).
- [11] C. Broholm *et al.*, Quantum spin liquids, *Science* **367**, 10.1126/science.aay0668 (2020).
- [12] J. R. Chamorro, T. M. McQueen, and T. T. Tran, Chemistry of quantum spin liquids, *Chemical Reviews* **121**, 10.1021/acs.chemrev.0c00641 (2020).
- [13] Y. Hashimoto, M. Wakeshima, and Y. Hinatsu, Magnetic properties of ternary sodium oxides NaLnO_2 (Ln = rare earths), *Journal of Solid State Chemistry* **176**, 266 (2003).
- [14] K. M. Ranjith *et al.*, Field-induced instability of the quantum spin liquid ground state in the $J_{\text{eff}}=1/2$ triangular-lattice compound NaYbO_2 , *Physical Review B* **99**, 180401(R) (2019).
- [15] L. Ding *et al.*, Gapless spin-liquid state in the structurally disorder-free triangular antiferromagnet NaYbO_2 , *Physical Review B* **100**, 144432 (2019).
- [16] M. Bordelon *et al.*, Field-tunable quantum disordered ground state in the triangular-lattice antiferromagnet NaYbO_2 , *Nature Physics* **15**, 1058 (2019).
- [17] M. Bordelon, C. Liu, L. Posthuma, P. M. Sarte, N. P. Butch, D. M. Pajerowki, A. Barnerjee, L. Balents, and S. D. Wilson, Spin excitations in the frustrated triangular lattice antiferromagnet NaYbO_2 , *Physical Review B* **101**, 224427 (2020).
- [18] J. Guo *et al.*, Magnetic-field and composition tuned antiferromagnetic instability in the quantum spin-liquid candidate NaYbO_2 , *Physical Review Materials* **4**, 064410 (2020).
- [19] M. Baenitz *et al.*, NaYbS_2 : A planar spin-1/2 triangular-lattice magnet and putative spin liquid, *Physical Review B* **98**, 220409(R) (2018).
- [20] Y. Jia *et al.*, Pressure induced insulator to metal transition in quantum spin liquid candidate NaYbS_2 , *Chinese Physics B* **32**, 096201 (2023).
- [21] R. Sarkar *et al.*, Quantum spin liquid ground state in the disorder free triangular lattice NaYbS_2 , *Physical Review B* **100**, 241116(R) (2019).
- [22] K. M. Ranjith *et al.*, Anisotropic field-induced ordering in the triangular-lattice quantum spin liquid NaYbSe_2 , *Physical Review B* **100**, 224417 (2019).
- [23] G. Lin *et al.*, Pressure-induced superconductivity in triangular lattice spin liquid candidate NaYbSe_2 , *Acta Physica Sinica* **72**, 157401 (2023).
- [24] Z. Zhang *et al.*, Crystalline electric field excitations in the quantum spin liquid candidate NaYbSe_2 , *Physical Review B* **103**, 035144 (2021).
- [25] Z. Zhang *et al.*, Low-energy spin dynamics of the quantum spin liquid candidate NaYbSe_2 , *Physical Review B* **106**, 085115 (2022).
- [26] P. Dai *et al.*, Spinon fermi surface spin liquid in a triangular lattice antiferromagnet NaYbSe_2 , *Physical Review X* **11**, 021044 (2021).
- [27] Y. Xu, Y. Sheng, and Y. Yang, Mechanism of the insulator-to-metal transition and superconductivity in the spin liquid candidate NaYbSe_2 under pressure, *NPJ Quantum Materials* **7**, 1 (2022).
- [28] Y. Jia *et al.*, Mott transition and superconductivity in quantum spin liquid candidate NaYbSe_2 , *Chinese Physics Letters* **37**, 097404 (2020).
- [29] T. Xie *et al.*, Complete field-induced spectral response of the spin-1/2 triangular-lattice antiferromagnet CsYbSe_2 , *NPJ Quantum Materials* **8**, 10.1038/s41535-023-00580-9 (2022).
- [30] R. Sereika *et al.*, Pressure-induced crystal structural and insulator-metal transitions in the quantum spin liquid candidate CsYbSe_2 , *Physical Review B* **108**, 174106 (2023).
- [31] J. Xing, L. D. Sanjeeva, J. Kim, G. R. Stewart, A. Podlesnyak, and A. S. Sefat, Field-induced magnetic transition and spin fluctuations in the quantum spin-liquid candidate CsYbSe_2 , *Physical Review B* **100**, 220407(R) (2019).
- [32] Y. Pai *et al.*, Mesoscale interplay between phonons and crystal electric field excitations in quantum spin liquid candidate CsYbSe_2 , *Journal of Materials Chemistry C* **10**, 10.1039/d1tc05934c (2022).
- [33] T. Xie *et al.*, Complete field-induced spectral response of the spin-1/2 triangular-lattice antiferromagnet CsYbSe_2 , *NPJ Quantum Materials* **8**, 10.1038/s41535-023-00580-9 (2022).
- [34] K. Somesh, S. S. Islam, S. Mohanty, G. Simutis, Z. Guguchia, C. Wang, J. Sichelschmidt, M. Baenitz, and R. Nath, Absence of magnetic order and emergence of unconventional fluctuations in the $J_{\text{eff}} = 1/2$ triangular-lattice antiferromagnet YbBO_3 , *Physical Review B* **107**, 064421 (2023).
- [35] G. Sala *et al.*, Structure and magnetism of the triangular lattice material YbBO_3 , *Journal of Physics Condensed Matter* **35**, 10.1088/1361-648X/ace147 (2023).
- [36] P. Mukherjee, Y. Wu, G. I. Lampronti, and S. E. Dutton, Magnetic properties of monoclinic lanthanide orthoborates, LnBO_3 , Ln = Gd, Tb, Dy, Ho, Er, Yb, *Materials Research Bulletin* **98**, 173 (2018).
- [37] X. Rao *et al.*, Survival of itinerant excitations and quantum spin state transitions in YbMgGaO_4 with chemical disorder, *Nature Communications* **12**, 1 (2021).
- [38] Y. Li, G. Chen, W. Tong, L. Pi, J. Liu, Z. Yang, X. Wang, and Q. Zhang, Rare-earth triangular lattice spin liquid: A single-crystal study of YbMgGaO_4 , *Physical Review Letters* **115**, 167203 (2015).
- [39] Y. Li *et al.*, Gapless quantum spin liquid ground state in the two dimensional spin-1/2 triangular antiferromagnet YbMgGaO_4 , *Scientific Reports* **5**, 16419 (2015).
- [40] J. A. M. Paddison *et al.*, Continuous excitations of the triangular-lattice quantum spin liquid YbMgGaO_4 , *Nature Physics* **13**, 117 (2016).
- [41] Y. Li, D. Adroja, R. I. Bewley, D. Voneshen, A. A. Tsirlin, P. Gegenwart, and Q. Zhang, Crystalline electric-field randomness in the triangular lattice spin-liquid YbMgGaO_4 , *Physical Review Letters* **118**, 107202 (2017).
- [42] Y. Shen *et al.*, Evidence for a spinon fermi surface in a triangular-lattice quantum-spin-liquid candidate, *Nature* **540**, 10.1038/nature20614 (2016).
- [43] S. Xu *et al.*, Realization of u(1) dirac quantum spin liquid in $\text{YbZn}_2\text{GaO}_5$ (2023).
- [44] U. K. Voma, S. Bhattacharya, E. Kermarrec, J. Alam, Y. M. Jana, B. Sana, P. Khuntia, S. K. Panda, and B. Koteswararao, Electronic structure and magnetic properties of the effective spin $J_{\text{eff}} = 1/2$ two-dimensional triangular lattice $\text{K}_3\text{Yb}(\text{VO}_4)_2$, *Physical Review B* **104**, 144411 (2021).
- [45] F. Song *et al.*, $\text{Ba}_6\text{RE}_2\text{Ti}_4\text{O}_{17}$ (RE= Nd, Sm, Gd, Dy–Yb): A family of quasi-two-dimensional triangular lattice magnets (2023).

- [46] J. Khatua, S. Bhattacharya, A. M. Strydom, A. Zorko, J. S. Lord, A. Ozarowski, E. Kermarrec, and P. Khuntia, Magnetic properties and spin dynamics in a spin-orbit driven $J_{\text{eff}}=1/2$ triangular lattice antiferromagnet, *Physical Review B* **109**, 024427 (2024).
- [47] T. Arh *et al.*, The ising triangular-lattice antiferromagnet neodymium heptatantalate as a quantum spin liquid candidate, *Nature Materials* **21**, 10.1038/s41563-021-01169-y (2022).
- [48] J. Xing, E. S. Choi, and R. Jin, Magnetic properties of layered CsNdSe_2 with triangular lattice, *APS Meeting Abstracts* (2023).
- [49] J. Xing *et al.*, Crystal synthesis and frustrated magnetism in triangular lattice CsRESe_2 ($\text{RE} = \text{La-Lu}$): Quantum spin liquid candidates CsCeSe_2 and CsYbSe_2 , *ACS Materials Letters* **2**, 71 (2020).
- [50] S. Zheng *et al.*, Exchange-renormalized crystal field excitations in the quantum ising magnet KTmSe_2 , *Physical Review B* **108**, 054435 (2023).
- [51] H. Bu *et al.*, Gapless triangular-lattice spin-liquid candidate in $\text{PrZnAl}_{11}\text{O}_{19}$, *Physical Review B* **106**, 134428 (2022).
- [52] Z. Ma *et al.*, Possible gapless quantum spin liquid behavior in the triangular-lattice ising antiferromagnet $\text{PrMgAl}_{11}\text{O}_{19}$, *Physical Review B* **109**, 10.1103/PhysRevB.109.165143 (2024).
- [53] S. Guo, A. Ghasemi, C. L. Broholm, and R. J. Cava, Magnetism on ideal triangular lattices in $\text{NaBaYb}(\text{BO}_3)_2$, *Physical Review Materials* **3**, 094404 (2019).
- [54] M. B. Sanders, F. A. Cevallos, and R. J. Cava, Magnetism in the $\text{KRE}(\text{BO}_3)_2$ ($\text{RE} = \text{Sm, Eu, Gd, Tb, Dy, Ho, Er, Tm, Yb, Lu}$) series: materials with a triangular rare earth lattice, *Materials Research Express* **4**, 036102 (2017).
- [55] B. L. Pan, J. M. Ni, L. P. He, Y. J. Yu, Y. Xu, and S. Y. Li, Specific heat and thermal conductivity of the triangular-lattice rare-earth material $\text{KBaYb}(\text{BO}_3)_2$ at ultralow temperature, *Physical Review B* **103**, 104412 (2021).
- [56] R. Bag *et al.*, Realization of quantum dipoles in triangular lattice crystal $\text{Ba}_3\text{Yb}(\text{BO}_3)_3$, *Physical Review B* **104**, 10.1103/PhysRevB.104.L220403 (2021).
- [57] A. O. Scheie *et al.*, Proximate spin liquid and fractionalization in the triangular antiferromagnet KYbSe_2 , *Nature Physics* **20**, 10.1038/s41567-023-02259-1 (2024).
- [58] A. O. Scheie *et al.*, Nonlinear magnons and exchange hamiltonians of the delafossite proximate quantum spin liquid candidates KYbSe_2 and NaYbSe_2 , *Physical Review B* **109**, 10.1103/PhysRevB.109.014425 (2024).
- [59] M. G. Kim *et al.*, Spin-liquid-like state in pure and mn-doped TbInO_3 with a nearly triangular lattice, *Physical Review B* **100**, 10.1103/PhysRevB.100.024405 (2019).
- [60] J. Kim *et al.*, Spin liquid state and topological structural defects in hexagonal TbInO_3 , *Physical Review X* **9**, 10.1103/PhysRevX.9.031005 (2019).
- [61] L. Clark *et al.*, Two-dimensional spin liquid behaviour in the triangular-honeycomb antiferromagnet TbInO_3 , *Nature Physics* **15**, 10.1038/s41567-018-0407-2 (2019).
- [62] M. Ye *et al.*, Crystal-field excitations and vibronic modes in the triangular-lattice spin-liquid candidate TbInO_3 , *Physical Review B* **104**, 10.1103/PhysRevB.104.085102 (2021).
- [63] T. S. Jung *et al.*, Unconventional room-temperature carriers in the triangular-lattice mott insulator TbInO_3 , *Nature Physics* **19**, 10.1038/s41567-023-02174-5 (2023).
- [64] F. A. Cavellos, K. Stolze, T. Kong, and R. J. Cava, Anisotropic magnetic properties of the triangular plane lattice material TmMgGaO_4 , *Materials Research Bulletin* **105**, 154 (2018).
- [65] Y. Shen *et al.*, Intertwined dipolar and multipolar order in the triangular-lattice magnet TmMgGaO_4 , *Nature Communications* **10**, 10.1038/s41467-019-12410-3 (2019).
- [66] C. Liu *et al.*, Intrinsic quantum ising model on a triangular lattice magnet TmMgGaO_4 , *Physical Review Research* **2**, 10.1103/PhysRevResearch.2.043013 (2020).
- [67] Z. Hu *et al.*, Evidence of the berezinskii-kosterlitz-thouless phase in a frustrated magnet, *Nature Communications* **11**, 1 (2020).
- [68] H. Li, Y. D. Liao, B. B. Chen, X. T. Zeng, X. L. Sheng, Y. Qi, Z. Y. Meng, and W. Li, Kosterlitz-thouless melting of magnetic order in the triangular quantum ising material TmMgGaO_4 , *Nature Communications* **11**, 1 (2020).
- [69] Z. Dun *et al.*, Neutron scattering investigation of proposed kosterlitz-thouless transitions in the triangular-lattice ising antiferromagnet TmMgGaO_4 , *Physical Review B* **103**, 10.1103/PhysRevB.103.064424 (2021).
- [70] B. A. Frandsen *et al.*, Investigating kosterlitz-thouless physics in the triangular lattice antiferromagnet TmMgGaO_4 , *Acta Crystallographica A* **77** (2022).
- [71] N. D. Kelly, C. Liu, and S. E. Dutton, Structure and magnetism of a new hexagonal polymorph of $\text{Ba}_3\text{Tb}(\text{BO}_3)_3$ with a quasi-2d triangular lattice, *Journal of Solid State Chemistry* **292**, 10.1016/j.jssc.2020.121640 (2020).
- [72] J. Xing *et al.*, Stripe antiferromagnetic ground state of the ideal triangular lattice compound KErSe_2 , *Physical Review B* **103**, 10.1103/PhysRevB.103.144413 (2021).
- [73] M. Ennis *et al.*, Realization of two-sublattice exchange physics in the triangular lattice compound $\text{Ba}_3\text{Er}(\text{BO}_3)_3$, *Communications Physics* **7**, 10.1038/s42005-024-01532-w (2024).
- [74] K. E. Avers, P. A. Maksimov, P. F. S. Rosa, S. M. Thomas, J. D. Thompson, W. P. Halperin, R. Movshovich, and A. L. Chernyshev, Fingerprinting triangular-lattice antiferromagnet by excitation gaps, *Physical Review B* **103**, L180406 (2021).
- [75] J. Lee *et al.*, The two-dimensional metallic triangular lattice antiferromagnet CeCd_3P_3 , *Physical Review B* **99**, 10.1103/PhysRevB.99.245159 (2019).
- [76] N. H. Jo *et al.*, Manipulating magnetism in the topological semimetal EuCd_2As_2 , *Physical Review B* **101**, 10.1103/PhysRevB.101.140402 (2020).
- [77] Y. Xu *et al.*, Unconventional transverse transport above and below the magnetic transition temperature in weyl semimetal EuCd_2As_2 , *Physical Review Letters* **126**, 10.1103/PhysRevLett.126.076602 (2021).
- [78] Y. Wang *et al.*, Long-time magnetic relaxation in antiferromagnetic topological material EuCd_2As_2 , *Chinese Physics Letters* **38**, 10.1088/0256-307X/38/7/077201 (2021).
- [79] Y. Sun *et al.*, Experimental evidence for field-induced metamagnetic transition of EuCd_2As_2 , *Journal of Rare Earths* **40**, 10.1016/j.jre.2021.08.002 (2022).

- [80] D. Santos-Cottin *et al.*, EuCd₂As₂: A magnetic semiconductor, *Physical Review Letters* **131**, 10.1103/PhysRevLett.131.186704 (2023).
- [81] R. P. Turcotte, J. Sawyer, and L. Eyring, On the rare earth dioxymonocarbonates and their decomposition, *Inorganic Chemistry* **8**, 238 (1968).
- [82] I. Kutlu and G. Meyer, Basische carbonate des dysprosiums: Dy₂O₂(CO)₃ und Dy(OH)(CO)₃, *Zeitschrift für anorganische und allgemeine Chemie* **625**, 402 (1999).
- [83] A. N. Christensen, Hydrothermal preparation of neodymium oxide carbonate, *Acta Chemica Scandinavica* **24**, 2440 (1970).
- [84] A. Olafsen *et al.*, On the crystal structure of Ln₂O₂CO₃ ii (Ln = La and Nd), *Journal of Solid State Chemistry* **158**, 10.1006/jssc.2000.9048 (2001).
- [85] Z. L. Dun *et al.*, Chemical pressure effects on magnetism in the quantum spin liquid candidates Yb₂X₂O₇ (X=Sn, Ti, Ge), *Physical Review B* **89**, 10.1103/PhysRevB.89.064401 (2014).
- [86] S. Calder *et al.*, A suite-level review of the neutron powder diffraction instruments at oak ridge national laboratory, *Review of Scientific Instruments* **89**, 10.1063/1.5033906 (2018).
- [87] M. B. Sanders *et al.*, Synthesis, crystal structure, and magnetic properties of novel 2d kagome materials RE₃Sb₃Mg₂O₁₄ (RE=La, Pr, Sm, Eu, Tb, Ho): Comparison to RE₃Sb₃Zn₂O₁₄ family, *Physica Status Solidi (b)* **253**, 2056 (2016).
- [88] Z. L. Dun *et al.*, Structural and magnetic properties of two branches of the tripod-kagome-lattice family A₂R₃Sb₃O₁₄ (A = Mg, Zn; R = Pr, Nd, Gd, Tb, Dy, Ho, Er, Yb), *Physical Review B* **95**, 104439 (2017).
- [89] J. Nagl *et al.*, Excitation spectrum and spin hamiltonian of the frustrated quantum ising magnet Pr₃BWO (2014).
- [90] J. G. Cheng *et al.*, High-pressure sequence of Ba₃NiSb₂O₉ structural phases: New s = 1 quantum spin liquids based on Ni²⁺, *Physical Review Letters* **107**, 10.1103/PhysRevLett.107.197204 (2011).
- [91] J. A. Quilliam *et al.*, Gapless quantum spin liquid ground state in the spin-1 antiferromagnet ₆HB-Ba₃NiSb₂O₉, *Physical Review B* **93**, 10.1103/PhysRevB.93.214432 (2016).
- [92] Y. Doi, Y. Hinatsu, and K. Ohoyama, Structural and magnetic properties of pseudo-two-dimensional triangular antiferromagnets Ba₃MSb₂O₉ (M=Mn, Co, and Ni), *Journal of Physics: Condensed Matter* **16**, 10.1088/0953-8984/16/49/009 (2004).
- [93] Y. Shirata *et al.*, Quantum magnetization plateau in spin-1 triangular-lattice antiferromagnet Ba₃NiSb₂O₉, *Journal of the Physical Society of Japan* **80**, 093702 (2011).
- [94] Y. Shirata, H. Tanaka, A. Matsuo, and K. Kindo, Experimental realization of a spin-1/2 triangular-lattice heisenberg antiferromagnet, *Physical Review Letters* **108**, 057205 (2012).
- [95] H. D. Zhou *et al.*, Successive phase transitions and extended spin-excitation continuum in the s = 1/2 triangular-lattice antiferromagnet Ba₃CoSb₂O₉, *Physical Review Letters* **109**, 267206 (2012).
- [96] T. Susuki *et al.*, Magnetization process and collective excitations in the s=1/2 triangular-lattice heisenberg antiferromagnet Ba₃CoSb₂O₉, *Physical Review Letters* **110**, 10.1103/PhysRevLett.110.267201 (2013).
- [97] A. Sera *et al.*, S=1/2 triangular-lattice antiferromagnets Ba₃CoSb₂O₉ and CsCuCl₃: Role of spin-orbit coupling, crystalline electric field effect, and dzyaloshinskii-moriya interaction, *Physical Review B* **94**, 10.1103/PhysRevB.94.214408 (2016).
- [98] Y. Kamiya *et al.*, The nature of spin excitations in the one-third magnetization plateau phase of Ba₃CoSb₂O₉, *Nature Communications* **9**, 10.1038/s41467-018-04914-1 (2018).
- [99] M. Li *et al.*, Magnetoelastic coupling and the magnetization plateau in Ba₃CoSb₂O₉, *Physical Review B* **99**, 10.1103/PhysRevB.99.094408 (2019).
- [100] N. A. Fortune *et al.*, Evolution of magnetic field induced ordering in the layered quantum heisenberg triangular-lattice antiferromagnet Ba₃CoSb₂O₉, *Physical Review B* **103**, 10.1103/PhysRevB.103.184425 (2021).
- [101] J. Kim *et al.*, Magnetic phase diagram of a 2-dimensional triangular lattice antiferromagnet Na₂BaMn(PO₄)₂, *Journal of Physics - Condensed Matter* **34**, 10.1088/1361-648X/ac965f (2022).
- [102] N. Li *et al.*, Quantum spin state transitions in the spin-1 equilateral triangular lattice antiferromagnet Na₂BaNi(PO₄)₂, *Physical Review B* **104**, 10.1103/PhysRevB.104.104403 (2021).
- [103] F. Ding *et al.*, Structure and frustrated magnetism of the two-dimensional triangular lattice antiferromagnet Na₂BaNi(PO₄)₂, *Chinese Physics B* **30**, 10.1088/1674-1056/abff1d (2021).
- [104] J. Sheng *et al.*, Two-dimensional quantum universality in the spin-1/2 triangular-lattice quantum antiferromagnet Na₂BaCo(PO₄)₂, *Proceedings of the National Academy of Sciences of the United States* **119**, 10.1073/pnas.2211193119 (2022).
- [105] N. Li *et al.*, Possible itinerant excitations and quantum spin state transitions in the effective spin-1/2 triangular-lattice antiferromagnet Na₂BaCo(PO₄)₂, *Nature Communications* **11**, 10.1038/s41467-020-18041-3 (2020).
- [106] J. Xing, L. D. Sanjeeva, A. F. May, and A. S. Sefat, Synthesis and anisotropic magnetism in quantum spin liquid candidates AYbSe₂ (A = K and Rb), *APL Materials* **9**, 111104 (2021).
- [107] M. Lee *et al.*, Series of phase transitions and multiferroicity in the quasi-two-dimensional spin-1/2 triangular-lattice antiferromagnet Ba₃CoNb₂O₉, *Physical Review B* **89**, 10.1103/PhysRevB.89.104420 (2014).
- [108] S. Lal *et al.*, Double magnetic transitions and exotic field-induced phase in the triangular lattice antiferromagnets Sr₃Co(Nb,Ta)₂O₉, *Physical Review B* **108**, 10.1103/PhysRevB.108.014429 (2023).
- [109] K. M. Ranjith *et al.*, Double phase transition in the triangular antiferromagnet Ba₃CoTa₂O₉, *Journal of Physics - Condensed Matter* **29**, 10.1088/1361-648X/aa57be (2017).
- [110] M. Lee *et al.*, Magnetic and electric properties of triangular lattice antiferromagnets Ba₃ATa₂O₉ (A = Ni and Co), *Materials Research Bulletin* **88**, 308 (2017).
- [111] Y. Kojima *et al.*, Quantum magnetic properties of the spin-1/2 triangular-lattice antiferromagnet Ba₂La₂CoTe₂O₁₂, *Physical Review B* **98**, 10.1103/PhysRevB.98.174406 (2018).
- [112] M. Saito *et al.*, Successive phase transitions and magnetization plateau in the spin-1 triangular-lattice antiferromagnet Ba₂La₂NiTe₂O₁₂ with small easy-axis

anisotropy, Physical Review B **100**, 10.1103/PhysRevB.100.064417 (2019).

- [113] H. Cho *et al.*, Studies on novel yb-based candidate triangular quantum antiferromagnets: $\text{Ba}_3\text{YbB}_3\text{O}_9$ and

$\text{Ba}_3\text{YbB}_9\text{O}_{18}$ (2021).